2016-06

Synthetic Jet and Turbulent Boundary Layer Interaction Quantification

Schatzman, David M.

AIAA Aviation 13-17 June 2016, Washington, D.C. 8th AIAA Flow Control Conference
http://hdl.handle.net/10945/50360

AIAA Aviation
13-17 June 2016, Washington, D.C.
8th AIAA Flow Control Conference

Synthetic Jet and Turbulent Boundary Layer Interaction Quantification

David M. Schatzman[1] and Jacob S. Wilson[1]
US Army Aviation Development Directorate
Aviation & Missile Research, Development & Engineering Center (AMRDEC)
Moffett Field, CA, 94035

and

M. S. Chandrasekhara[2]
Naval Postgraduate School, Monterey, CA, 93943

An experimental effort was performed in order to identify and quantify the structural changes to a two-dimensional turbulent boundary layer under the influence of a high spanwise aspect ratio slot synthetic jet. A comprehensive test matrix of key synthetic jet variables including non-dimensional stroke length, jet Reynolds number, and slot angle, was conducted in quiescent air, zero pressure gradient, and a mild adverse pressure gradient turbulent boundary layer flows. Time averaged and phase averaged features of the modified boundary layer flowfield were examined using hot-wire anemometry. Velocity profiles and turbulence data measured downstream of the actuator were compared for the range of actuator parameters with the baseline turbulent boundary layers.

Nomenclature

C_f	=	skin friction coefficient
$C_{f,2}$	=	turbulent contribution to skin friction coefficient
C_p	=	pressure coefficient
f	=	actuator frequency
h	=	slot width
H	=	boundary layer shape factor
$K_{u,v}$	=	anisotropy coefficient
L_o	=	stroke length
Re_x	=	Reynolds number based on streamwise distance
Re_θ	=	Reynolds number based on momentum thickness
Re_o	=	synthetic jet Reynolds number
T	=	actuator period
u_τ	=	wall-shear velocity
U_o	=	average jet velocity
U_e	=	local external velocity
U_∞	=	freestream velocity
u',v'	=	turbulent velocity fluctuations
x, y, z	=	coordinates distance

[1] Research Engineer, U.S. Army Aviation Development Directorate, NASA Ames Research Center, Mail Stop 215-1, Member AIAA.
[2] Research Professor, Department of Mechanical & Aerospace Engineering, NASA Ames Research Center, Mail Stop 215-1, Associate Fellow AIAA

α_{jet} = synthetic jet angle with respect to the wall
β = pressure gradient parameter
δ = boundary layer thickness
δ^* = boundary layer displacement thickness
θ = boundary layer momentum thickness
ν = kinematic viscosity
ϕ = actuator phase angle
τ = actuator half cycle
τ_w = wall shear stress
AFC = active flow control
APG = adverse pressure gradient
ZPG = zero pressure gradient

I. Introduction

THE expansion of performance flight envelopes through adverse force reduction using AFC has been a goal in the fixed wing and rotorcraft fields for many years. Recent experimental and computational efforts have shown the possible performance benefits of several AFC devices[1,2]. One of the most studied active flow control device is the synthetic jet or zero-net mass flux jet. Substantial work has been done to characterize isolated synthetic jets in still air and the interaction of synthetic jets with a cross flow. This work has been reviewed in detail by Glezer and Amitay[3]. Typically comparisons of synthetic jets are conducted by using non-dimensional actuator parameters such as the jet Reynolds number and the stroke length[4].

Examples of applications using synthetic jets to control aerodynamic flows are abound in the literature. Zhang and Zhong[5] investigated turbulent boundary layer separation control with an array of circular orifice synthetic jets over a two dimensional ramp section. This work showed that the reduced frequency parameter was a key factor in determining effective flow control. Wilson et al.[6] showed that on a simple NACA 0036 airfoil the location and even the angle of the synthetic jets to the aerodynamic surface were found to be prime drivers of system effectiveness. Kim et al.[7] showed that the synthetic jet exit configuration changes the vortical structures and is therefore an important component in effective momentum transfer for separation control. In a more applied configuration, Schaeffler et al.[8] showed drag and download reduction with synthetic jet excitation on a rotorcraft fuselage under the influence of a rotor. Synthetic jet actuators have also been flight tested for download reduction on a XV-15 tiltrotor aircraft during hover.[9]

There have been additional studies that characterize the interaction of a synthetic jet actuator with a canonical flat plate turbulent boundary layer. Schaeffler and Jenkins[10] produced a detailed dataset of an isolated synthetic jet with a turbulent boundary layer crossflow for validation with active flow control simulations. Jabbal and Zhong[11] investigated the near wall effect of circular orifice synthetic jet in a boundary layer and characterized the different vortical structures resulting from the flow control parameter space. Smith[12] studied the interaction of a turbulent boundary layer and an array of synthetic jet slots with both streamwise and spanwise configuration. The spanwise slot configuration produced a blockage effect on the boundary layer, while the streamwise oriented slots produced longitudinal vortices embedded in the boundary layer. Detailed work by Keirsbulck et al.[13] considered the effect of steady blowing on Reynolds stress and the turbulent structure in the near wall region.

In a real world application of AFC on an aircraft, actuators will be operated in an adverse pressure gradient as the turbulent boundary layer approaches separation. There have been numerous studies of APG turbulent boundary layers that document fundamental differences when compared to a ZPG flow. For example, the experiments of Skare and Krogtrad[14] in an equilibrium APG boundary layer, and the studies of Spalart and Watmuff[15], both document the characteristic increase of the boundary layer shape factor, H, in the presence of an adverse pressure gradient, and the development of secondary turbulence intensity peak, which develops above the near-wall peak. The Reynolds stress distribution is considerably different across the boundary layer with the maximum Reynolds stress also shifted away from the wall, towards the middle of the boundary layer.

The main objective of the current work is to identify and quantify changes to the structure of both a ZPG and APG turbulent boundary layer generated by synthetic jet actuator (SJA) flow control for a range of actuator parameters and slot geometries. The expectation is that such changes serve as markers to identify and devise proper (successful) implementation of the technique for any application. Such predictability requires a clear and deep understanding of the turbulent boundary layer flow physics in the vicinity of, and under the influence of, the synthetic jet. The ultimate goal is to uncover this understanding and apply it towards developing predictable and reliable flow control methods for a specific flow situation.

II. Experimental Setup

Investigations were conducted in a low-speed turbulent boundary layer wind tunnel, a U.S. Army Aviation Development Directorate facility at NASA Ames Research Center. The tunnel has a 9 ft long test section that is 3 ft wide with an entrance height of 1ft. The boundary layer was tripped at the test section entrance then free to develop along a smooth aluminum floor. The flexible ceiling also allows for a ZPG and an APG configuration. Freestream turbulence levels in the center of the ZPG test section are less than 0.1% for frequencies above 1 Hz. The streamwise pressure gradient was set to zero by slightly diverging the flexible ceiling plate to account for boundary layer growth. An adverse pressure gradient was established with an s-shape contour over the length of the test section. A schematic of the wind tunnel test section for these two configurations is shown in Figure 1. Static pressure taps along the centerline of the test section floor and at several spanwise locations were used to verify the pressure gradient and flow uniformity. The centerline pressure distributions for ZPG and APG configurations are shown in Figure 2.

A two-dimensional traverse system is mounted above the slotted test section ceiling for measurement of velocity profiles using single and two-component hot-wire probes. A TSI IFA300 constant-temperature hot-wire anemometer system and TSI Model 1218-T1.5 and 1243-T1.5 boundary layer probes, were used to measure velocity profiles in detailed streamwise planes. These probes have a wire diameter of 0.00015 in and a sensing length of 0.05 in. The hot-wire time series was acquired for a sample time ranging from 3.28 to 26.21 seconds at a sample rate of 40 kHz and low-pass filtered at 20 kHz.

A TSI Model 1129 Automatic Calibrator was used for calibration of hot-wires over the full range of expected velocities. The x-wires were calibrated for 11 different yaw angles over a range of -30° to 30°, at four calibration velocities. Two fourth-order polynomials were used to fit the velocity versus voltage curves, and yaw coefficients were calculated for each yaw velocity. Freestream temperature was acquired with each data point and used for temperature correction. Therefore given a recorded voltage pair, the cooling velocities and resulting u-v velocity components could be calculated[16].

Figure 3 presents baseline velocity profiles for the ZPG and APG configurations measured 60 in downstream of the boundary layer trip. For ZPG measurements conducted at U_e = 53.9 ft/s, the boundary layer thickness was δ = 1.08 in, displacement thickness was δ^* = 0.163 in, shape factor H = 1.39, and $\mathrm{Re}_\theta \approx 3220$. The measurements were consistent with a canonical ZPG turbulent boundary layer. For the APG measurements the external freestream velocity at this location was U_e = 51.7 ft/s, the boundary layer thickness almost doubles to δ = 1.97 in, displacement thickness grows to δ^* = 0.514 in, shape factor becomes H = 1.72, and $Re_\theta \approx 7900$. At this location the pressure gradient parameter $\beta = (\delta^*/\tau_w)\mathrm{d}P/\mathrm{d}x$ = 1.83, which corresponds to a mild adverse pressure gradient flow[17]. The Clauser chart method was used to estimate the friction velocity for not only the ZPG profile but also the APG case since the pressure gradient parameter $\beta < 2$.

At the halfway point along the test section a bank of six voice coil type synthetic jet actuators are installed in a single cavity below the test section floor as shown schematically in Figure 4. The coordinate system for the actuator boundary layer interaction measurements is defined such that the origin is located at the center of SJA slot on the center of the lower wall; where x is the streamwise direction, y is the vertical direction from the wall, and z is the spanwise direction from the center-line. The actuator cavity is covered with an aluminum plate with inserts for various exit slot geometries of a continuous spanwise width of h = 0.06 in and depth of 0.125 in. A Pragmatic 2714A 20MS/s waveform generator was used to apply an AC signal to the actuators. The driving sinusoidal waveform was sent to a Peavey GPS 3500 power amplifier to boost the input power. This stereo amplifier has a total harmonic distortion less than 0.1% and a slew rate of 40 V/s. A voltmeter was used to verify the voltage output to the actuators, and the current was measured with a Pearson current monitor, Model 2100. The actuator cavity pressure was measured using an unsteady differential pressure sensor with the reference open to the lab ambient pressure. The waveform generator signal was recorded and used as a reference for phase averaged hot-wire velocity measurements.

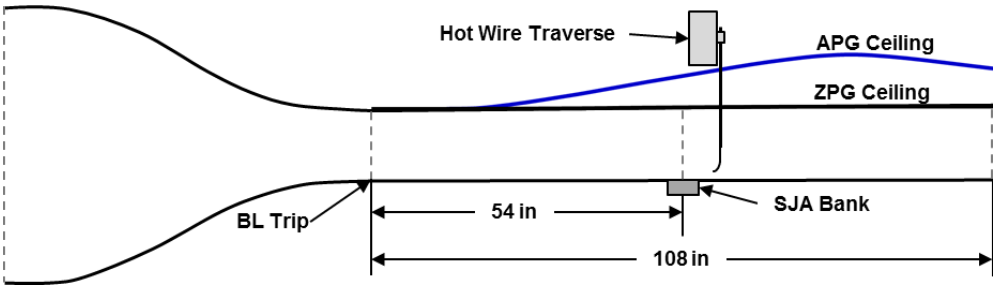

Figure 1. Schematic of wind tunnel test section.

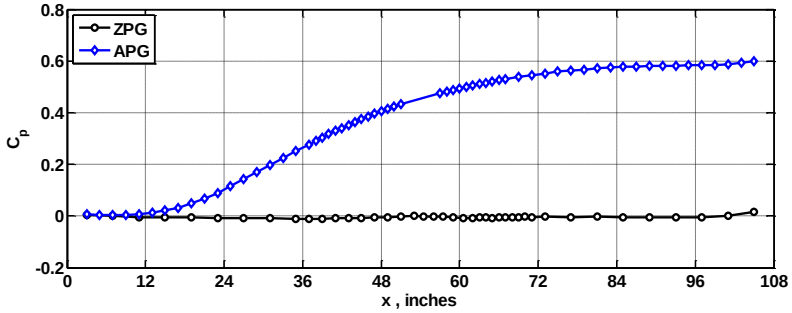

Figure 2. Streamwise pressure gradient for two different ceiling configurations.

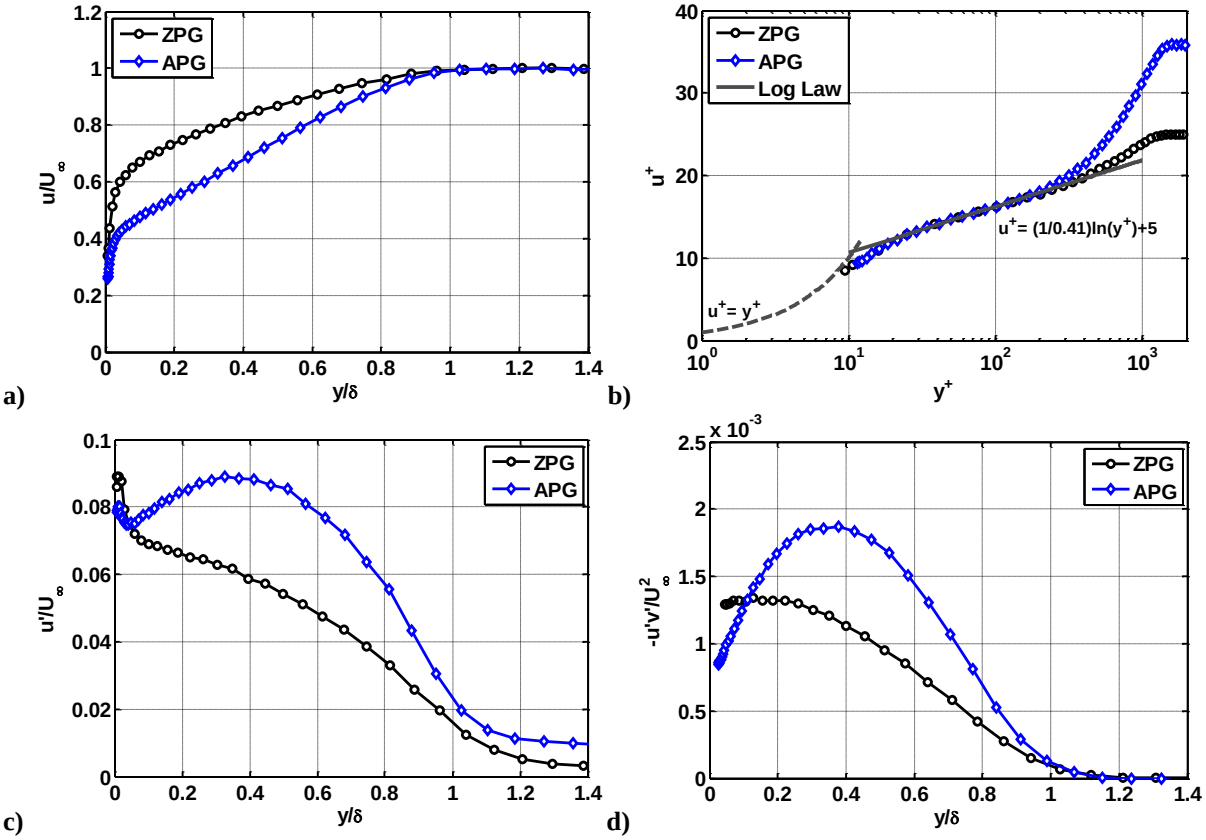

Figure 3. Baseline boundary layer profiles at x = 60 inches for ZPG and APG; a) outer variable velocity profiles b) inner variable velocity profiles c) turbulence intensity and d) turbulent Reynolds stress.

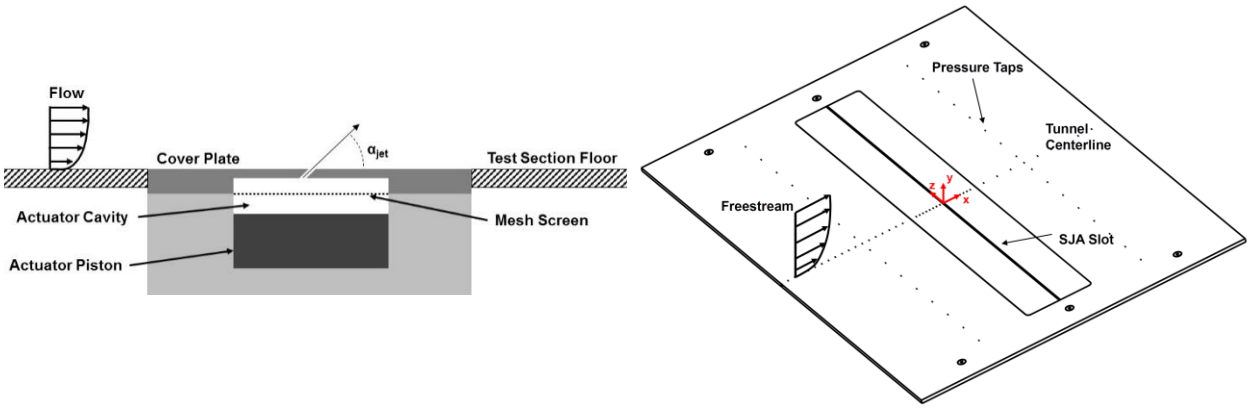

Figure 4. Schematics of synthetic jet actuator spanwise slot and coordinate system.

III. SJA Characterization

The characterization and calibration of the synthetic jet was accomplished by traversing a miniature hot-wire across the exit plane of a 90 degree slot. The two main jet parameters controlled in the experiments were the non-dimensional stroke length, L_o/h, and the jet Reynolds number, Re_o. To define these quantities, the periodic jet velocity is spatially-averaged across the exit plane by,

$$u_o(t) = \int_{-0.5}^{+0.5} u(x/h, t)\, d(x/h) \tag{1}$$

where h is the width of the exit slot. The stroke length is defined by

$$L_o = \int_0^{\tau} u_o(t)\, dt \tag{2}$$

where $\tau = T/2$, $T = 1/f$, and f is the set actuator frequency. The jet Reynolds number is defined as

$$\mathrm{Re}_o = \frac{U_o h}{\nu} \tag{3}$$

where ν is the kinematic viscosity, and U_o is the average jet velocity defined as

$$U_o = \frac{L_o}{T}\,. \tag{4}$$

Figure 5 shows measurements of the time-averaged jet velocity across the slot width, and spatially-averaged velocity during the blowing half cycle for to a 10 volt, f = 120 Hz actuator setting. A test matrix with the actuator settings and resulting measured parameters for α_{jet} = 90° slot configuration are summarized in Table 1. The selected settings were used for each slot angle and were used to independently test and compare the effect of non-dimensional stroke length, L_o/h, and jet Reynolds number, Re_o. The chosen settings were bounded by the operating limits of the actuation system, which has a preferred frequency of f = 120 Hz. Included in the table for reference is measured power consumption for each actuator setting.

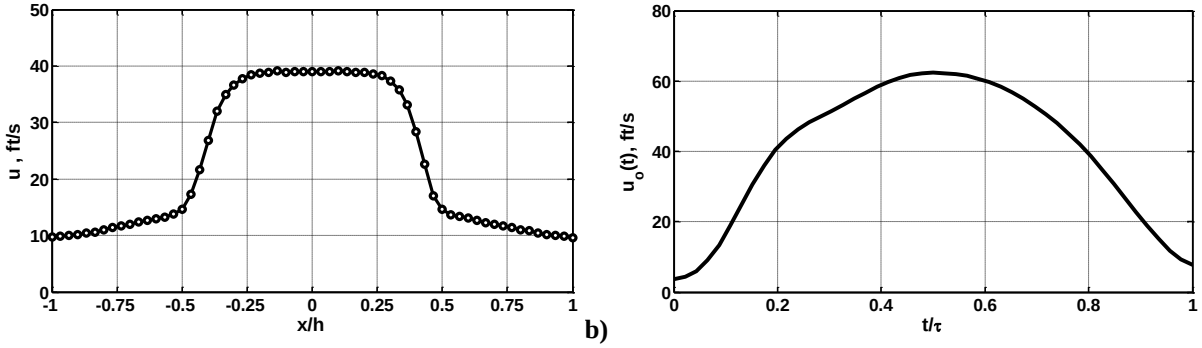

Figure 5. Synthetic jet characterization for α_{jet} = 90° a) time-averaged jet velocity across slot width and b) spatially-averaged velocity during blowing half cycle.

Table 1: Synthetic Jet Parameter Test Matrix

Voltage	f , Hz	U_o , ft/s	L_o/h	Re_o	Watts
5.0	50.0	8.0	31.8	253	11.2
10.0	120.0	21.4	35.6	680	45.5
13.4	200.0	19.6	19.6	623	102.1
20.0	172.3	29.6	34.4	943	211.6
14.1	60.0	21.3	71.0	678	55.8

IV. Results and Discussion

A. Quiescent Air

Hot-wire measurements of the velocity field in quiescent air were conducted over the range of synthetic jet parameters with various slot geometries. Figure 6 shows time averaged velocity fields of the α_{jet} = 90° slot for similar stroke lengths of L_o/h = 31.8-35.6, and increasing jet Reynolds number. It is clear that when the velocity field is non-dimensionalized by the average jet velocity U_o, the flow fields show a similar pattern, with only slightly increasing jet expansion with Reynolds number. With the jet Reynolds number fixed in the range of Re_o = 623-680, Figure 7 shows the phase averaged velocity field at the peak blowing portion of the cycle. As expected, the jet column height increases with stroke length.

Figure 8 shows the resulting time averaged velocity fields when the slot angle is reduced from α_{jet} = 90° and asymmetry is introduced. The formation of asymmetric vortices causes the jet to turn at an angle less than the slot angle and eventually convect downstream along the horizontal surface. Figure 9 shows that with the slot angle fixed at α_{jet} = 45°, and similar jet Reynolds numbers, the increasing stroke length plays an important role in the velocity magnitude pattern. The lowest stroke length results in the largest time averaged velocity magnitude since each high frequency jet pulse remains in the measurement plane before the subsequent pulse. As the stroke length is increased, the actuator frequency is reduced, and the unsteady jet is convected farther downstream during the actuation cycle, out of the measurement plane. This results in a lower time averaged velocity for the same fixed measurement plane.

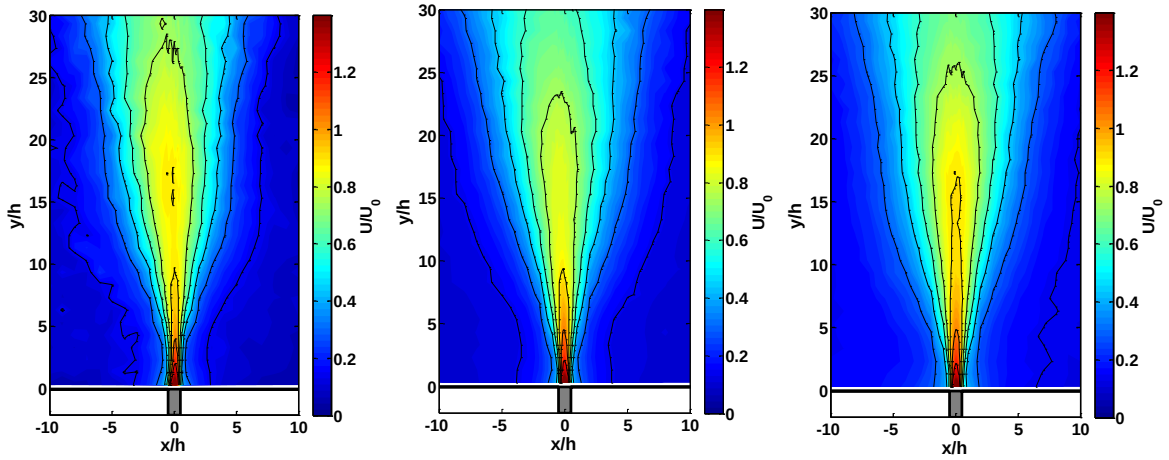

a) Re_o = 253 **b) Re_o = 680** **c) Re_o = 943**

Figure 6. Time averaged velocity field in quiescent air with 90° slot and L_o/h = 31.8-35.6, for various Re_o.

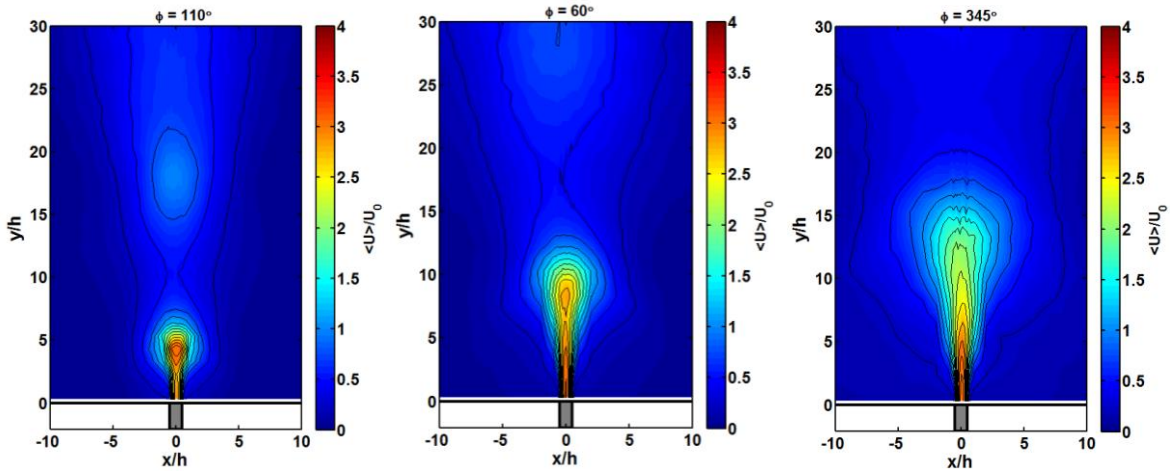

a) L_o/h = 19.6 **b) L_o/h = 35.6** **c) L_o/h = 71.0**

Figure 7. Phase averaged velocity at peak blowing with 90° slot and Re_o = 623-680, for various stroke lengths.

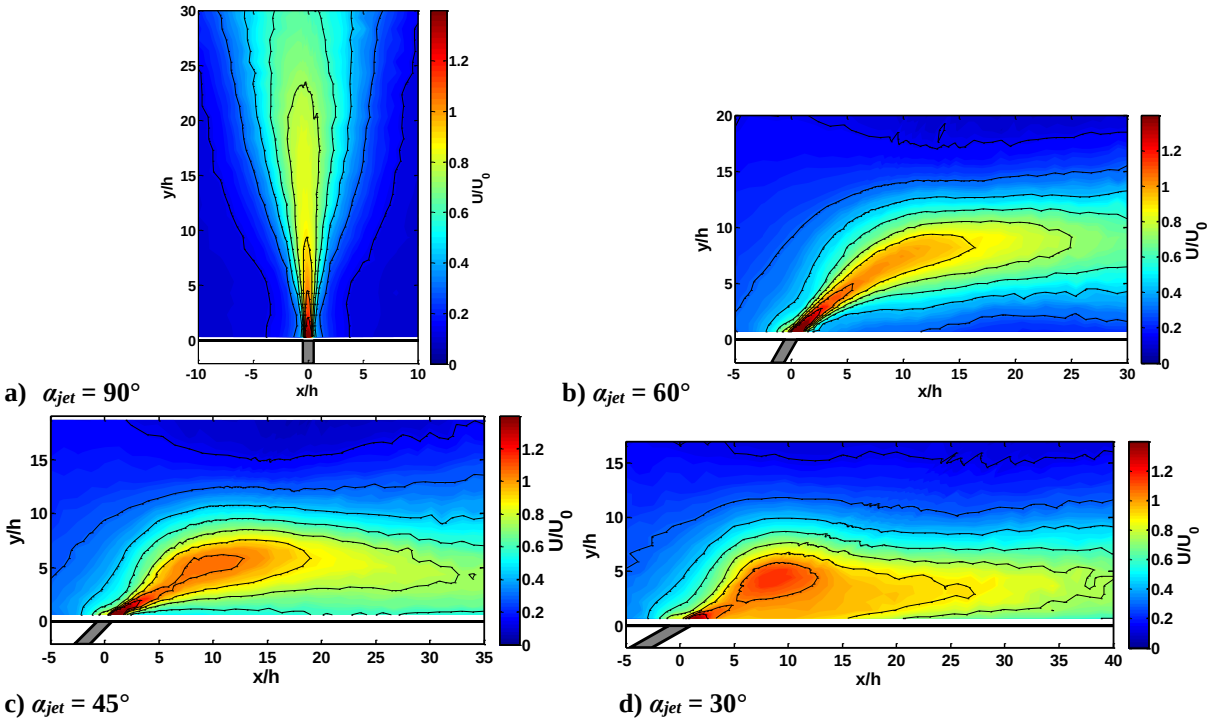

Figure 8. Time averaged velocity field in quiescent air with L_o/h = 35.6 and Re_o = 680, for various slot angles.

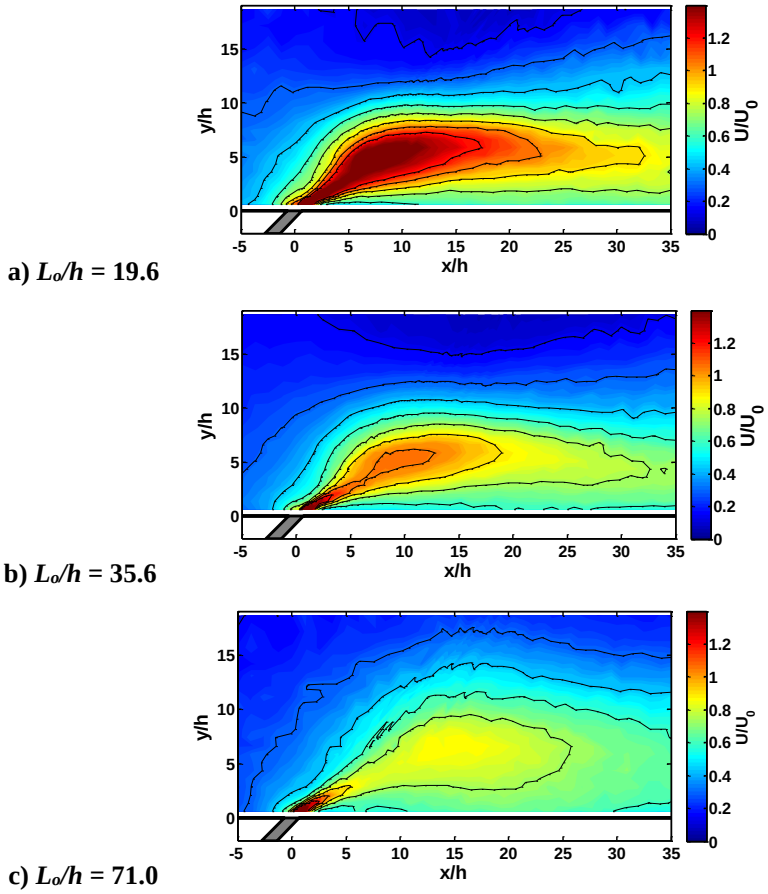

Figure 9. Time averaged velocity in quiescent air with 45° slot and Re_o = 623-680, for various stroke lengths.

B. Zero Pressure Gradient Turbulent Boundary Layer

1. *Slot Angle Effect - ZPG*

Velocity measurements were conducted over the range of synthetic jet parameters and slot geometries in the turbulent boundary layer wind tunnel for ZPG flow at Re_θ = 3200, and Re_x = 1.5 x 10^6, where the characteristic length scale, x = 54 in, is the distance from the boundary layer trip at the start of the test section to the center of the actuator slot. Figure 10 shows the time average velocity flowfield measurements obtained with an x-wire for various SJA slot angle with actuator settings of L_o/h = 35.6 and Re_o = 680. For the α_{jet} = 90° slot angle, Figure 10a, the time average velocity field shows that the jet spreads away from the wall and extends to the outer portion of the boundary layer; there is little momentum transfer in the near wall region. However, the angled slots result in an attached wall jet and increased momentum in the lower portion of the boundary layer. This slot angle effect is also shown in the Reynolds stress contours in Figure 11.

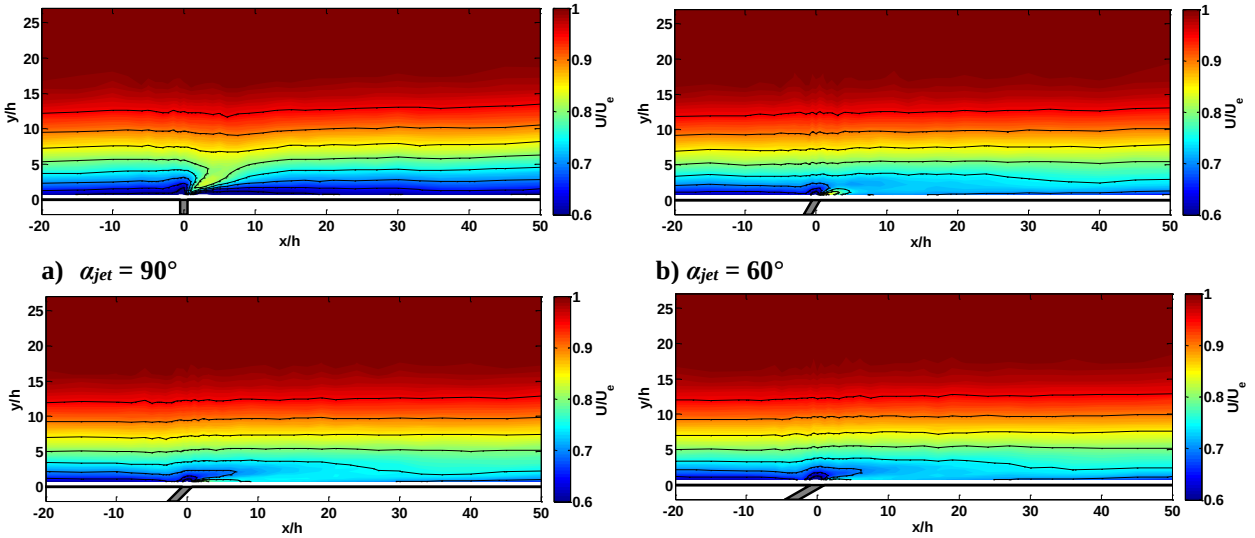

Figure 10. Effect of slot angle on time averaged velocity field for ZPG with L_o/h = 35.6 and Re_o = 680.

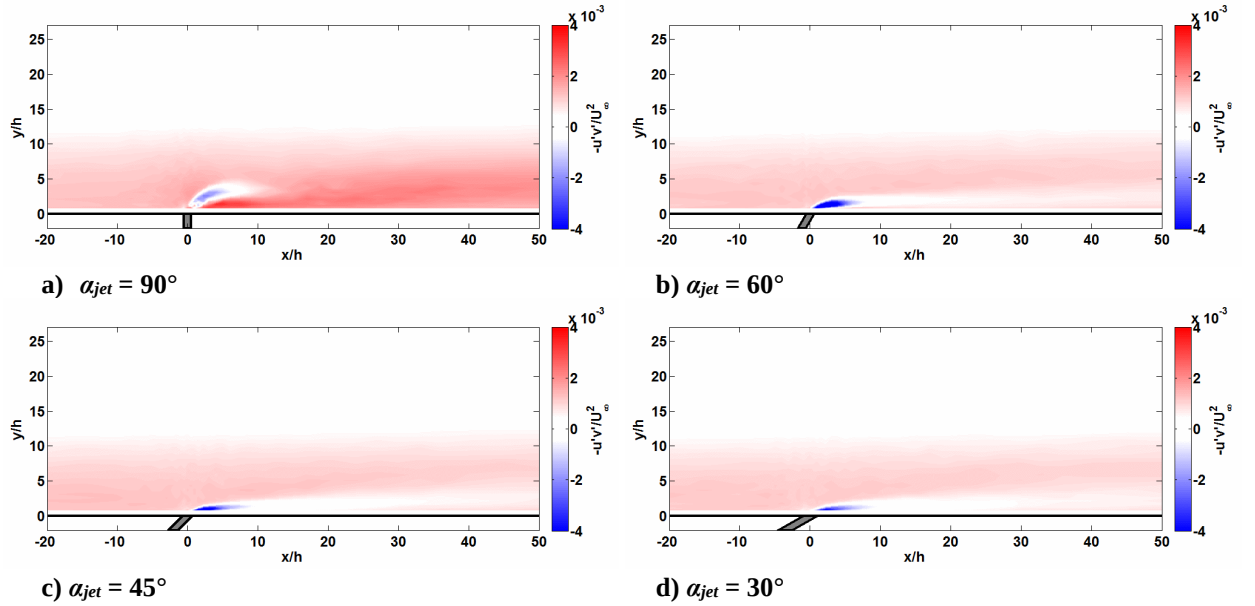

Figure 11. Effect of slot angle on Reynolds stress for ZPG with L_o/h = 35.6 and Re_o = 680.

Time averaged profiles 50 slot widths downstream of the actuator are shown in Figure 12. The velocity profiles are plotted with outer and inner variables. The wall-shear velocity, u_τ , used for inner variable scaling was obtained using the Clauser chart method from the baseline data. This baseline value was used to normalize the velocity data for each of the controlled cases. Note that streamwise turbulence intensity and Reynolds stress profiles have coherent fluctuations removed from the turbulent statistics. Each of the profiles for the SJA with angled slots have similar behavior. The velocity profiles show added momentum in the near wall region, which correspond to reduced turbulence and Reynolds stress in that region. The velocity profile for the 90° degree slot is similar to the baseline case, and the turbulence and Reynolds stress increase in the lower 50% of the boundary layer.

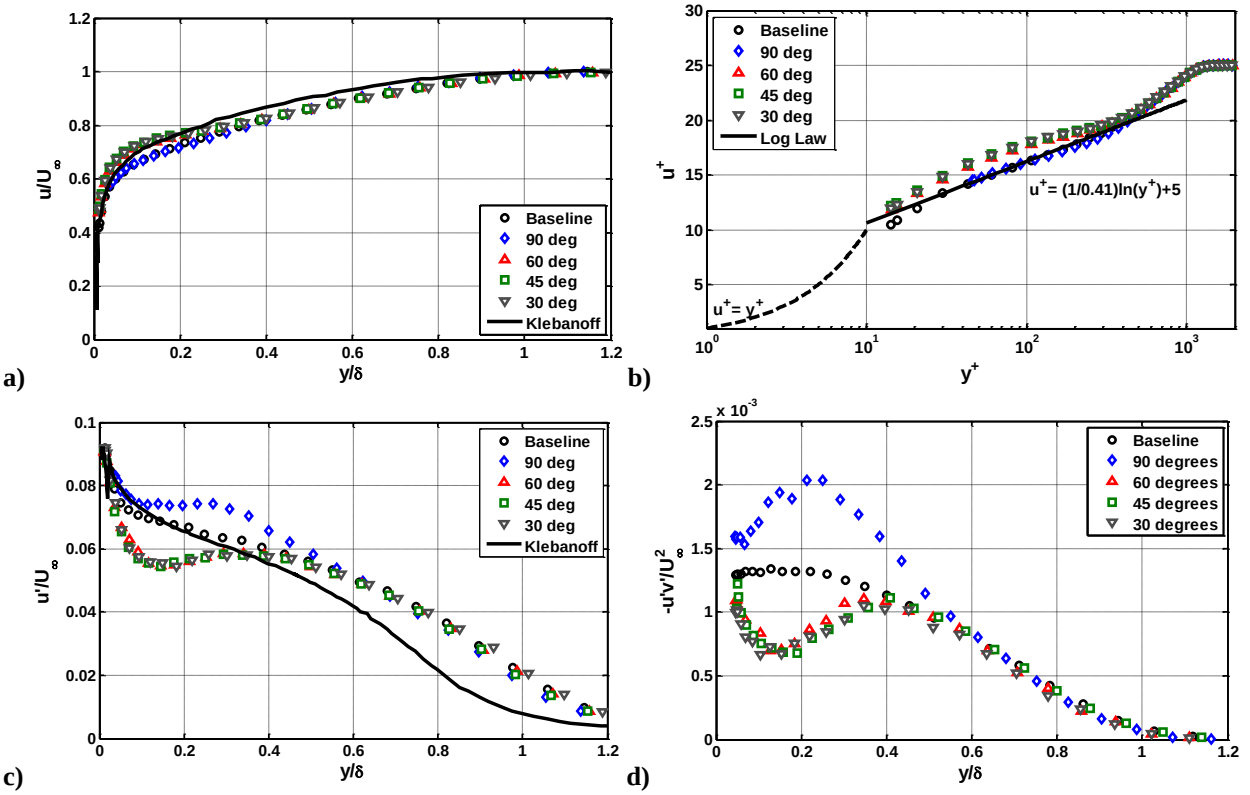

Figure 12. Effect of slot angle on time averaged boundary layer measurements at *x/h* = 50 for ZPG with L_o/h = 35.6 and Re_o = 680; a) outer variable velocity profiles b) inner variable velocity profiles c) turbulence intensity d) Reynolds stress profiles.

2. Jet Reynolds number and Stroke length effect - ZPG

The effect of jet Reynolds number on time averaged ZPG boundary layer profiles at *x/h* = 50 for the slot with α_{jet} = 45°, and a fixed range of non-dimensional stroke length, L_o/h = 31.8-35.6, is shown in Figure 13. It is clear from the inner variable profiles, at this downstream location, that the momentum addition to the near wall region increases with increasing jet Reynolds number. The corresponding decrease in the Reynolds stress is consistent with the formation of an attached wall jet as the velocity gradients increase with jet Reynolds number. A comparison of different non-dimensional stroke lengths at a fixed Re_o = 623-680 is shown in Figure 14. The controlled velocity profiles show little variation for the range of L_o/h tested. The Reynolds stress reduction region shows a weak but noticeable trend toward zero with increasing stroke length.

The streamwise effect on the displacement thickness, δ^*, due to increasing jet Reynolds number is shown in Figure 15a. For the largest jet Reynolds number Re_o = 943, at a streamwise location 120 slot widths downstream of the actuator, the displacement thickness is reduced by 22% compared to the baseline case. Figure 15b shows a slight trend of displacement thickness reduction with increasing stroke length, which mirrors the trend seen in the Reynolds stress profiles.

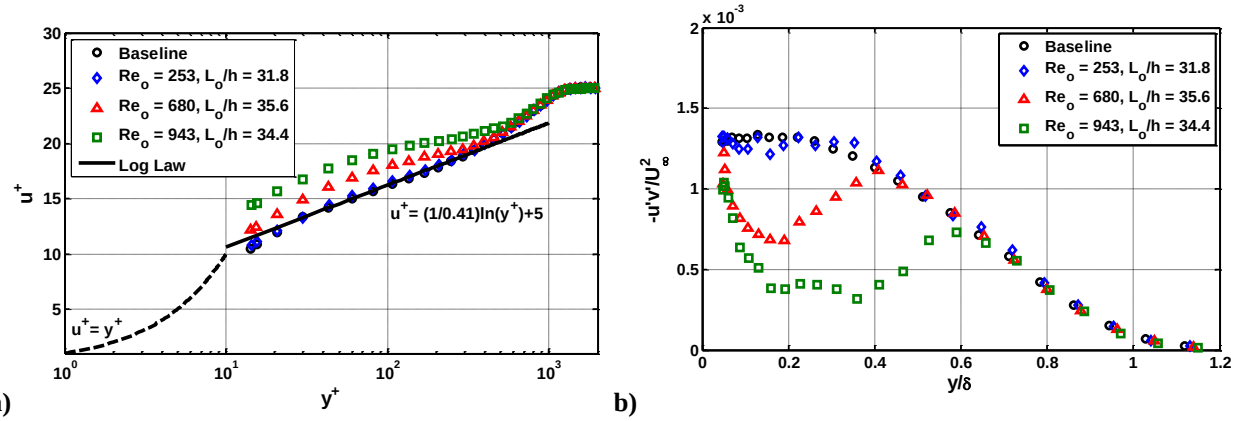

Figure 13. Effect of jet Reynolds number on time averaged boundary layer profiles at *x/h* = 50 for ZPG with 45 degree slot, and *Lo/h* = 31.8-35.6; a) inner variable velocity profiles b) Reynolds stress profiles.

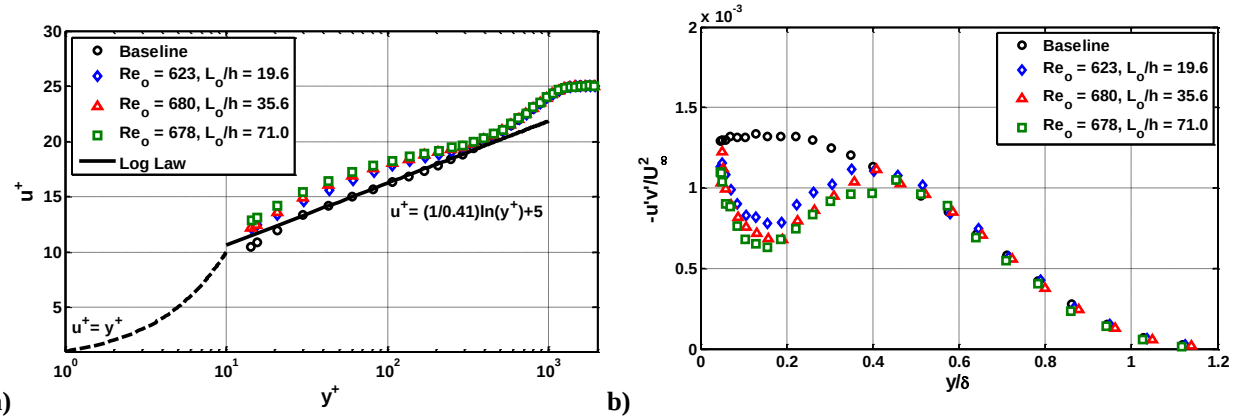

Figure 14. Effect of stroke length on time averaged boundary layer profiles at *x/h* = 50 for ZPG with 45 degree slot, and *Reo* = 623-680; a) inner variable velocity profiles b) Reynolds stress profiles.

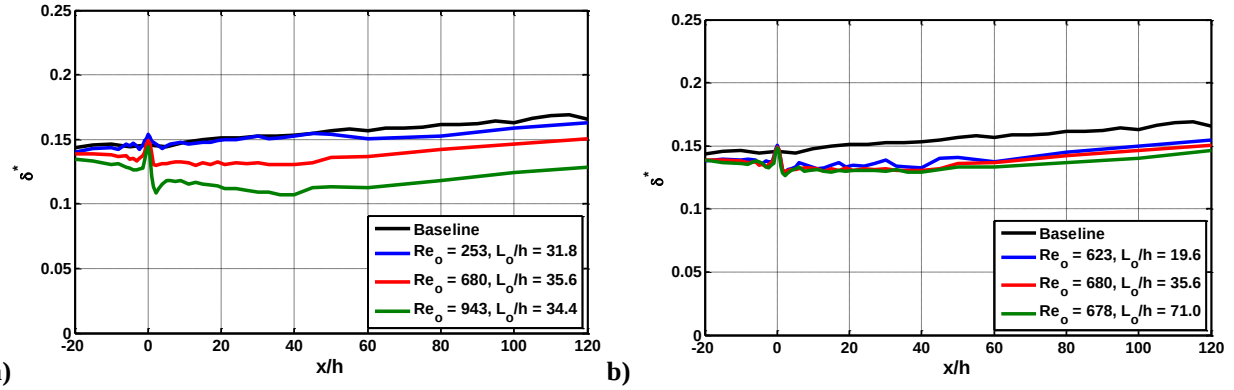

Figure 15. Streamwise variation of displacement thickness for ZPG showing the effect of a) *Reo* and b) *Lo/h*.

3. Phase Averaged Velocity Field - ZPG

The measured velocity signal and the actuator input signal were recorded simultaneously, which allows for a phase reference of the unsteady flow-field. Data was reduced using a triple decomposition $u(t) = \bar{u} + \tilde{u}(t) + u'(t)$, where $\bar{u}$ is the time average velocity, $\tilde{u}(t)$ is the periodic component, and $u'(t)$ random turbulent component[18]. The phase average velocity $\langle u(\phi) \rangle$ was calculated using a peak detection algorithm to identify each actuation cycle. Data for each cycle was divided into 72 individual bins corresponding to a given phase angle, $\Delta\phi = 5°$, over the unsteady

actuation cycle. Figure 16 shows a typical sequence of the velocity field for a 45 degree slot with synthetic jet parameters of L_o/h = 35.6, and Re_o = 680. The sequence captures the peak blowing portion of the cycle at $\phi = 40°$, and the flowfield at peak suction at ϕ = 220°.

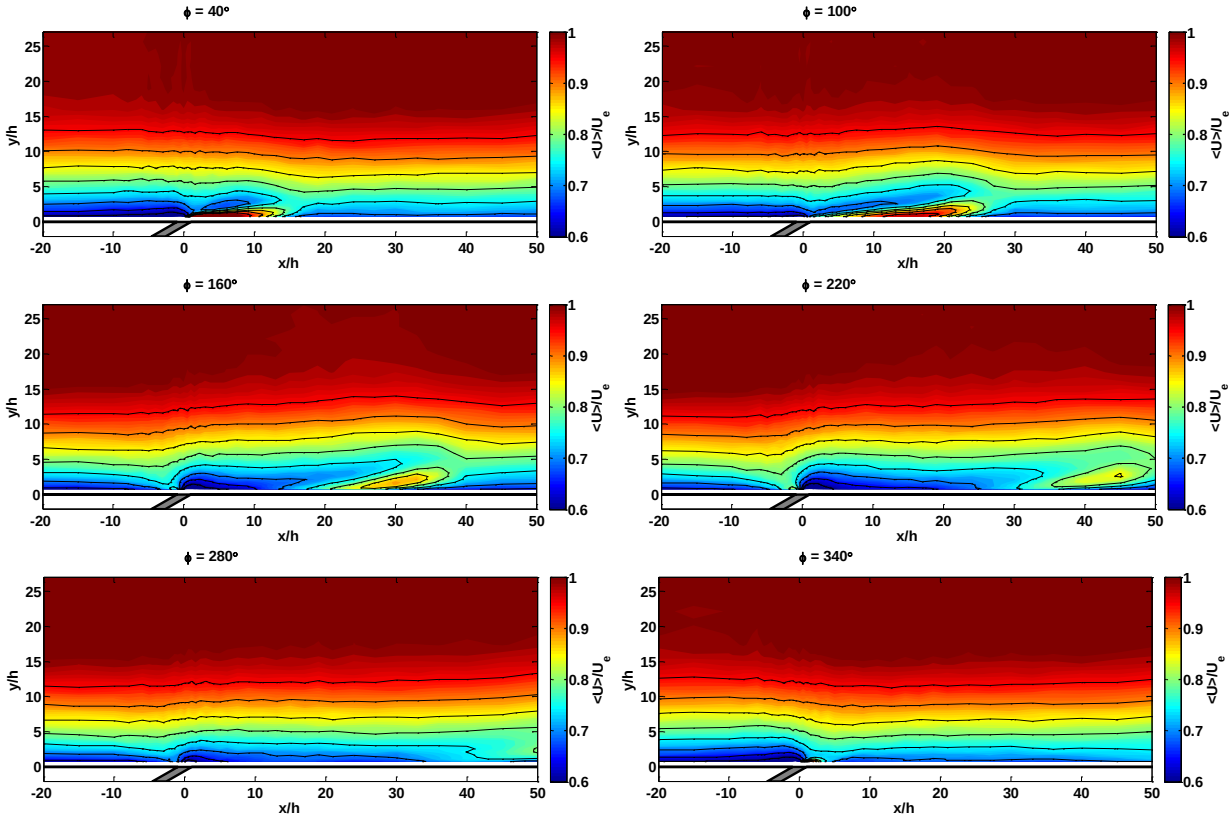

Figure 16. Phase averaged velocity fields for ZPG, 45° slot, L_o/h = 35.6, and Re_o = 680.

C. Adverse Pressure Gradient Turbulent Boundary Layer

Measurements of the SJA/boundary layer interaction were repeated for the APG configuration. The APG turbulent boundary layer flow measurements were conducted for $Re_x = 2.0 \times 10^6$, where the characteristic length scale, x = 54 in, is the distance from the boundary layer trip at the start of the test section to the center of the actuator slot, and the freestream velocity was measured at the entrance of the test section with the pitot-static probe. This freestream condition at the test section entrance corresponds to a similar velocity ratio at the actuator under the APG, when compared to the ZPG case. The Reynolds number based on the measured momentum thickness at the actuator was Re_θ = 6880.

1. Slot Angle Effect – APG

The effect of slot angle on time averaged velocity flowfield is shown in Figure 17 for an actuator setting of L_o/h = 35.6 and Re_o = 680. The α_{jet} = 90° slot angle shows the time averaged jet acts like a fence which produces a blockage effect on the boundary layer flow, which transfers momentum to the outer portion of the boundary layer. There is little momentum transfer toward the near wall region and minimal change to the downstream boundary layer flow. The angled slots result in near wall momentum addition both upstream and downstream of the slot. Far downstream of the slot, x/h = 40-50, the angled slots results in a similar flowfield with momentum addition in the lower 25% of the boundary layer. Figure 18 shows the effect of the slot angles on the Reynolds stress contours. There is increased Reynolds stress downstream of the α_{jet} = 90° slot and reduced Reynolds stress downstream of the angled slots. These findings are also shown in the time averaged profiles at x/h = 50 in Figure 19. The inner scaling velocity profiles show that the results of the 90° slot are similar to the baseline measurements at this location, and the angled slot profiles collapse to a common curve, with increased skin friction. The turbulence intensity profiles show an

increase slightly above the baseline case for the 90° slot, while the angled slots result in reduced turbulence intensity in the lower 40% of the boundary layer.

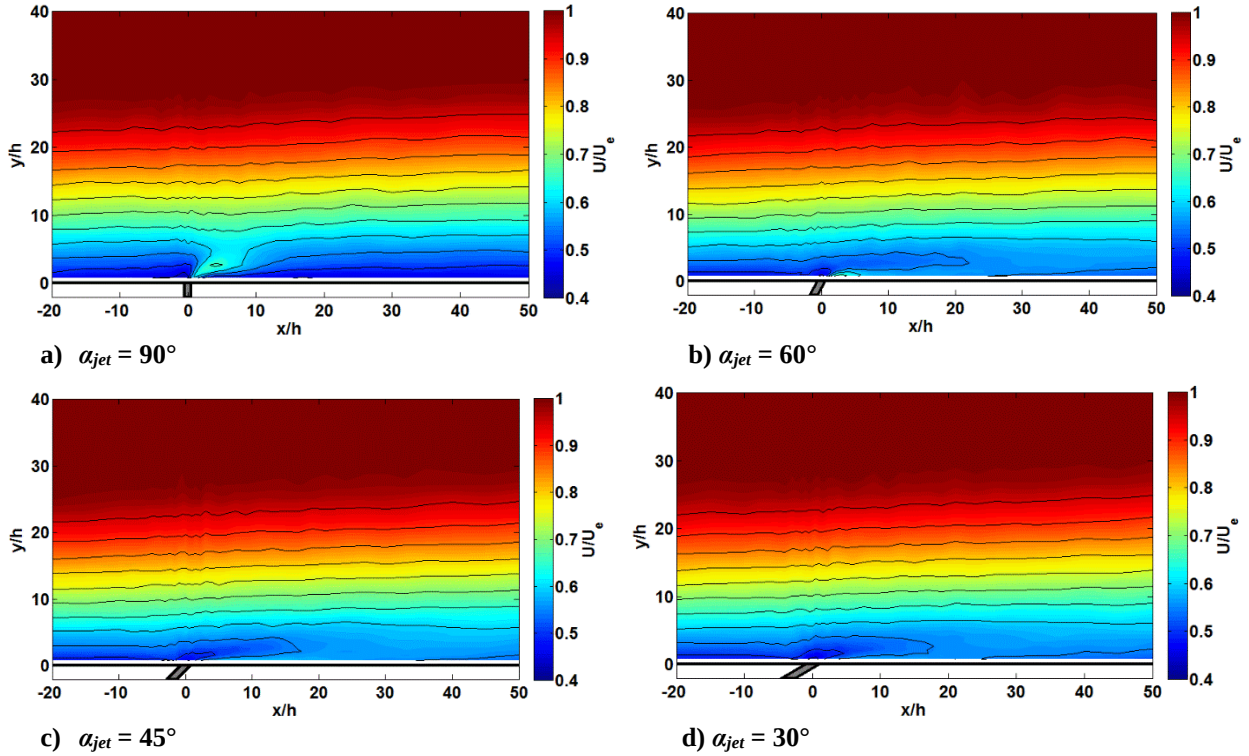

Figure 17. Effect of slot angle on time averaged velocity for APG with L_o/h = 35.6 and Re_o = 680.

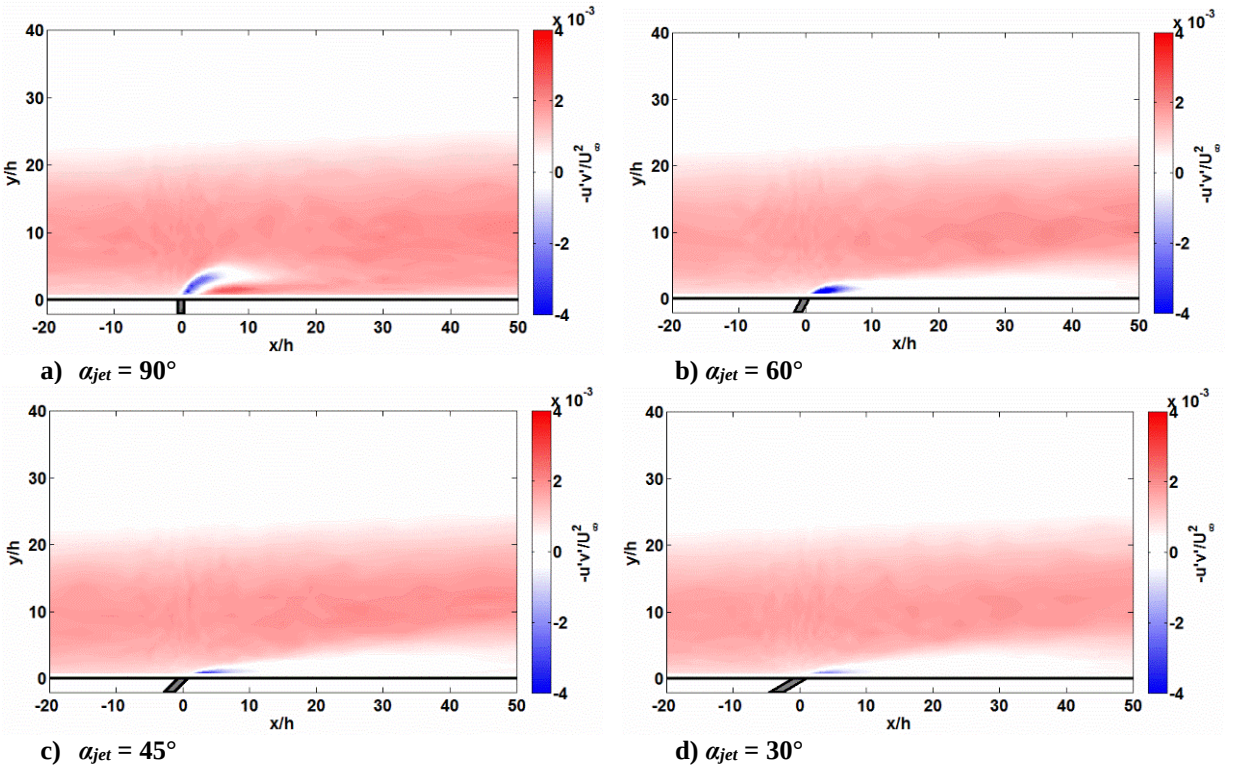

Figure 18. Effect of slot angle on Reynolds stress for APG with L_o/h = 35.6 and Re_o = 680.

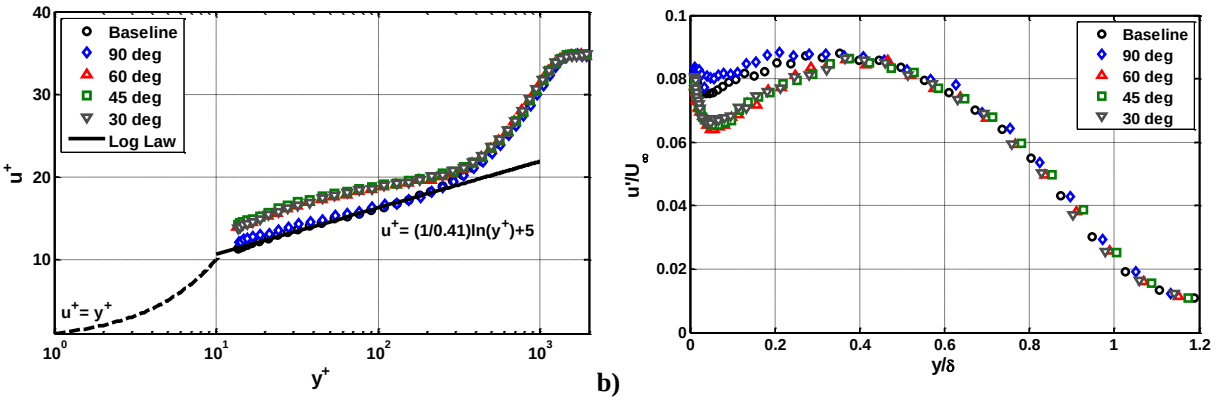

Figure 19. Effect of slot angle on time averaged boundary layer measurements at *x/h* = 50 for APG with *L*$_o$*/h* = 35.6 and *Re*$_o$ = 680; a) inner variable velocity profiles b) Reynolds stress profiles.

2. Jet Reynolds number and Stroke length effect - APG

Figure 20 shows the effect of jet Reynolds number on time averaged APG boundary layer velocity profiles for the slot with α_{jet} = 45°, and a fixed range of non-dimensional stroke length, *L*$_o$*/h* = 31.8-35.6. The outer variable scaled profiles shows increased momentum addition in the near wall region as the actuator control authority is increased through the jet Reynolds number at this streamwise location, *x/h* = 50. For the inner variable scaling, scaled by the friction velocity of the baseline case, Figure 20b shows that the increased jet Reynolds number is consistent with an increase in the skin friction at this downstream location.

Figure 21a shows the dramatic effect the jet Reynolds number has on the Reynolds stress distribution. For the largest jet Reynolds number, *Re*$_o$ = 943, shows significant reduction of the Reynolds stress for the lower half of the boundary layer. In fact, the minimum value of the Reynolds stress is still less than zero at *y/δ* = 0.2, even 50 slot widths downstream due to the velocity gradients associated with the strong wall jet for this actuator setting.

The effect of the increasing jet Reynolds number on the anisotropy coefficient is shown in Figure 21a. The anisotropy coefficient is defined as $K_{u,v} = \left(u'^2 - v'^2\right)/\left(u'^2 + v'^2\right)$, and is typically maximum in the near wall region where most of the turbulent energy is produced. Keirsbulck et al.[13] showed that steady blowing resulted in significant reduction in the anisotropy coefficient in the near-wall region. Similarly here, the synthetic jet unsteady excitation results in a reduction of anisotropy in the near wall region. For the highest jet Reynolds number the anisotropy coefficient is reduced over the entire lower half of the APG boundary layer.

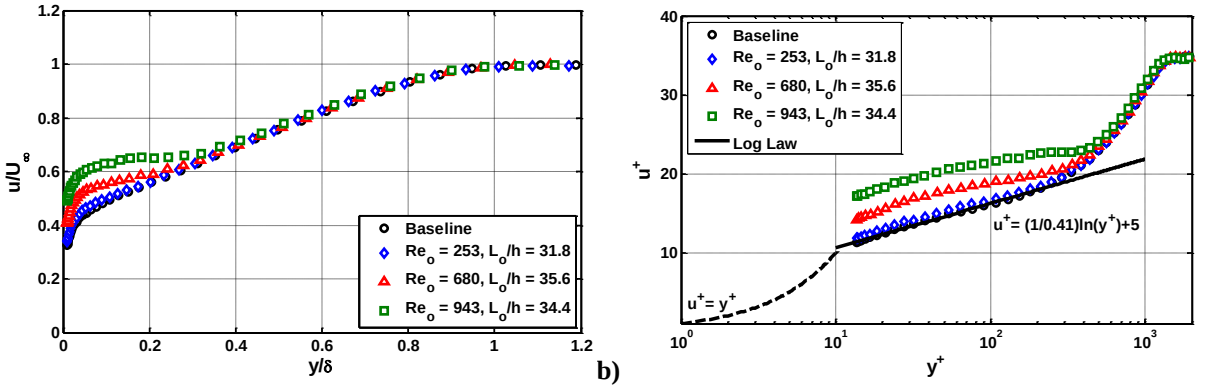

Figure 20. Effect of jet Reynolds number on time averaged boundary layer profiles at *x/h* = 50 for APG with 45 degree slot, and *L*$_o$*/h* = 31.8-35.6; a) outer variable velocity profiles and b) inner variable velocity profiles.

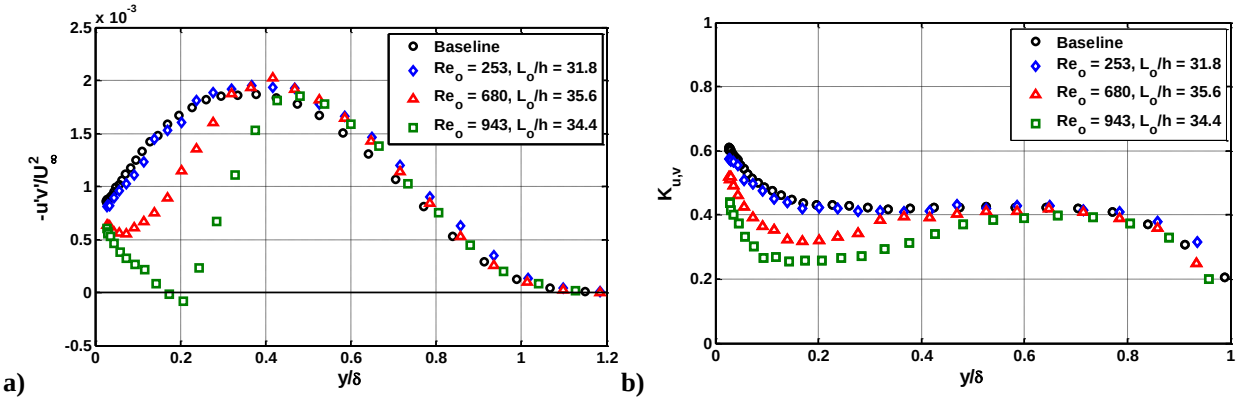

a) b)

Figure 21. Effect of jet Reynolds number on time averaged boundary layer profiles for APG on a) Reynolds stress profiles b) anisotropy coefficient.

The velocity and Reynolds stress profiles of the APG boundary layer controlled with a range of non-dimensional stroke lengths at a fixed Re_o = 623-680 is shown in Figure 22. Velocity profiles show a slight increase in near wall momentum addition with increasing L_o/h, and the near wall Reynolds stress reduces with increasing stroke length. The streamwise development on the boundary layer shape factor, $H = \delta^*/\theta$, for the range of non-dimensional actuator parameters is shown in Figure 23. The maximum shape factor reduction occurs at x/h = 36, for the largest jet Reynolds number Re_o = 943, and corresponds to a 12% reduction compared to the baseline case. Figure 15b shows that downstream of actuation the reduction is shape factor tracks with increasing stroke length.

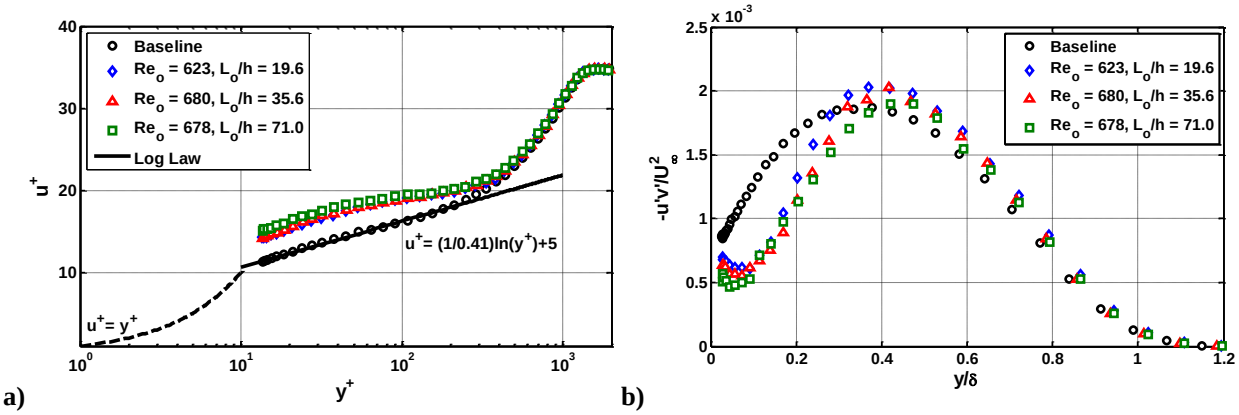

a) b)

Figure 22. Effect of stroke length on time averaged boundary layer profiles at x/h = 50 for APG with 45 degree slot, and Re_o = 623-680; a) inner variable velocity profiles b) Reynolds stress profiles.

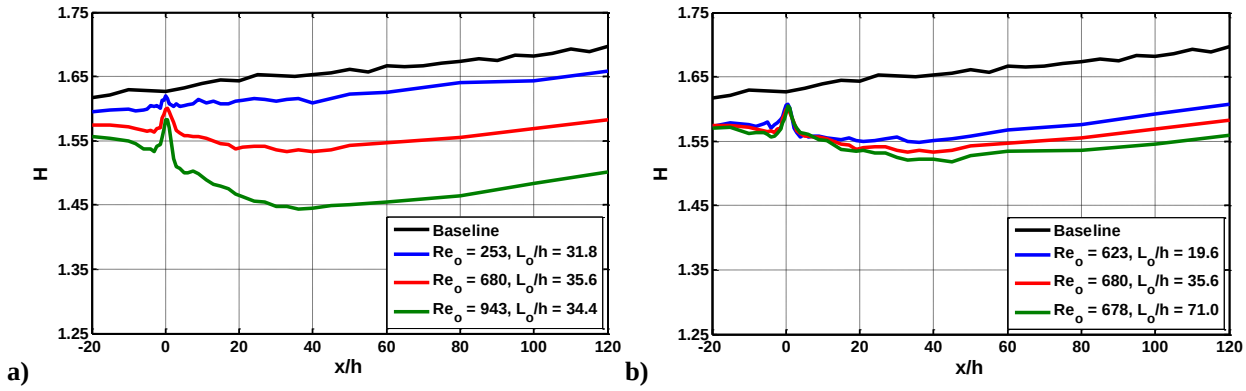

a) b)

Figure 23. Streamwise variation of shape factor for APG showing the effect of a) Re_o and b) L_o/h.

3. Freestream Reynolds number variation - APG

With the SJA parameters fixed at L_o/h = 35.6 and Re_o = 680 for the α_{jet} = 45° slot, the freestream velocity was varied for the APG configuration. The significant effect the freestream Reynolds number has on the time averaged velocity field, for fixed control authority, is shown in Figure 24. Not only does the increased velocity ratio result in substantial momentum addition downstream of the actuator for reduced freestream velocities, but there is also significant thinning of the boundary layer upstream of the slot due to the increased velocity ratio during the suction phase of the synthetic jet actuation cycle. These finding are also illustrated in the streamwise development of the shape factor shown in Figure 25. For the lowest freestream velocity the synthetic jet excitation reduces the baseline APG shape factor downstream of the actuator by 20.4%, resulting in a value below that of the baseline ZPG turbulent boundary layer.

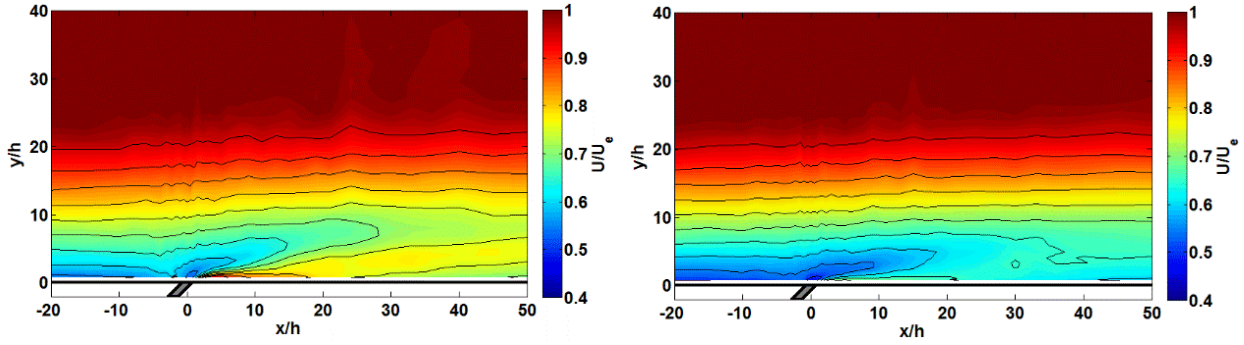

a) Re_θ **= 3850** **b)** Re_θ **= 5200**

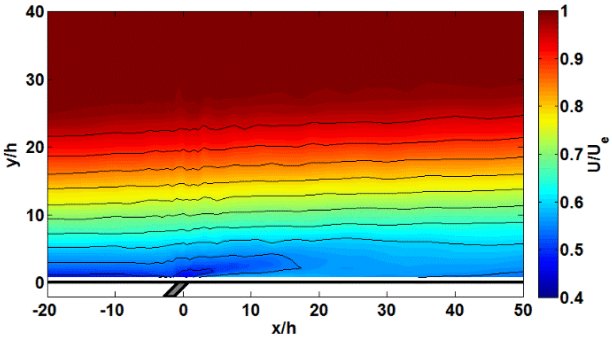

c) Re_θ **= 7370**

Figure 24. Effect of freestream Reynolds number on velocity field for APG with L_o/h = 35.6 and Re_o = 680.

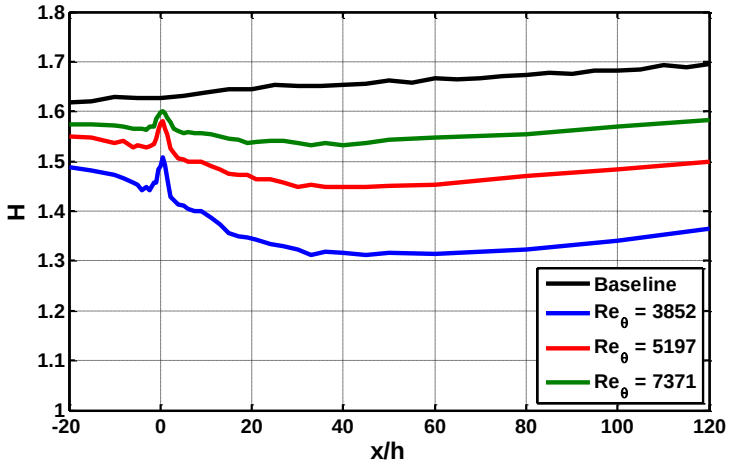

Figure 25. Variation of shape factor for APG with increasing freestream Reynolds number for a fixed actuator setting of L_o/h = 35.6 and Re_o = 680.

This effect of the freestream Reynolds number is also presented in the time averaged boundary layer profiles at x/h = 50, with fixed actuator authority in Figure 26. These trends are similar to the findings with fixed freestream velocity and increasing jet Reynolds number. The velocity profiles clearly illustrate the reduced momentum addition as the freestream velocity is increased. The relative strength and size of the time averaged wall jet is shown in the Reynolds stress profiles for each velocity setting. The extent of the reduction in anisotropy coefficient develops from the near wall region and the lower 40% of the boundary layer for the highest external velocity, to throughout the entire boundary layer height for the lowest freestream velocity setting.

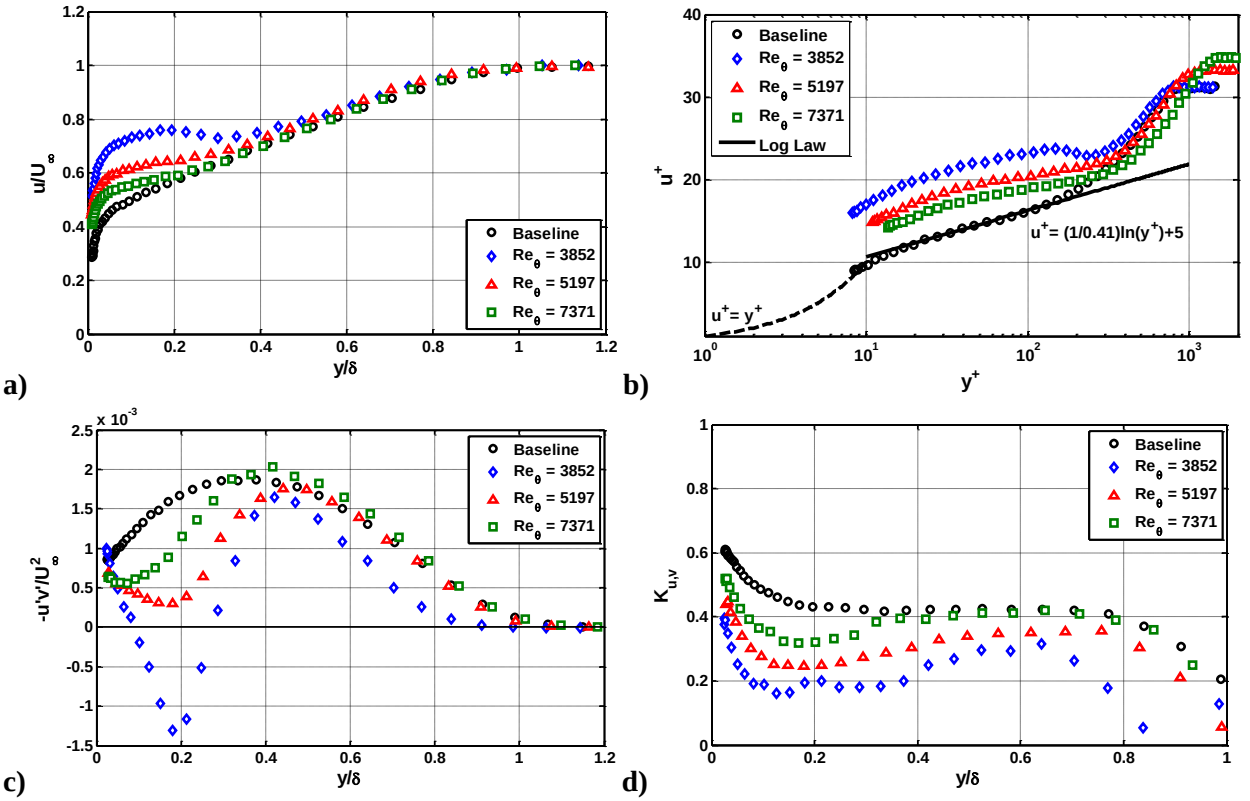

Figure 26. Effect of freestream Reynolds number on time averaged profiles at x/h = 50 for APG with L_o/h = 35.6 and Re_o = 680; a) outer variable velocity profiles b) inner variable velocity profiles c) Reynolds stress d) anisotropy coefficient.

4. *Phase Averaged Velocity Field - APG*

The phase-averaged velocity field with respect to the actuator input signal is presented as a sequence in Figure 27 for the APG turbulent boundary layer with the 45 degree slot L_o/h = 35.6 and Re_o = 680. The peak blowing portion of the cycle occurs at ϕ = 40°, and the wall jet then convects downstream for subsequent phase angles and eventually lifts up away from the wall. A pocket of low momentum fluid from upstream of the slot is lifted off the wall and convects downstream along the top of the convected front of the jet. The flowfield at ϕ = 220° shows boundary layer thinning upstream of the actuator slot due to the suction portion of the cycle.

Figure 28 shows the phase averaged velocity and Reynolds stress profiles measured at x/h = 50. The plotted phase angles represent the typical bounds of the profiles for the actuation cycle. For the inner velocity scaling presented in Figure 28a, the friction velocity used for scaling was based on the baseline velocity data. Since the variation of the velocity profiles at this measurement location and for this actuator setting was minimal, the Clauser chart method was also applied to each controlled profile for the unsteady actuation cycle. The resulting estimate of the skin friction coefficient as a function of phase is presented in Figure 29. The phase averaged skin friction coefficient shows a positive offset from the baseline value, C_f = 0.00165, and a sinusoidal variation throughout the phase.

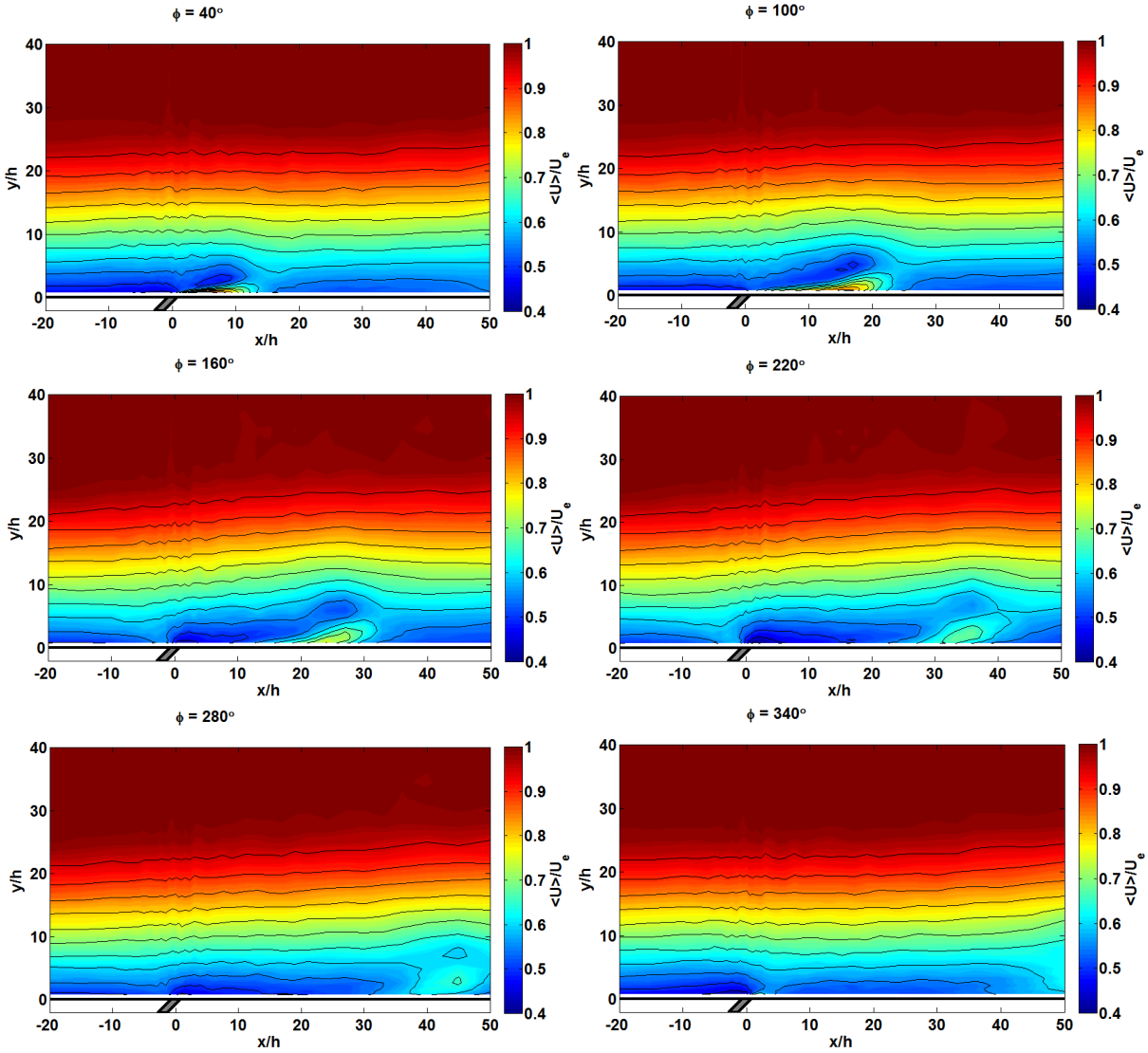

Figure 27. Phase averaged velocity fields for APG, 45° slot, L_o/h = 35.6, and Re_o = 680.

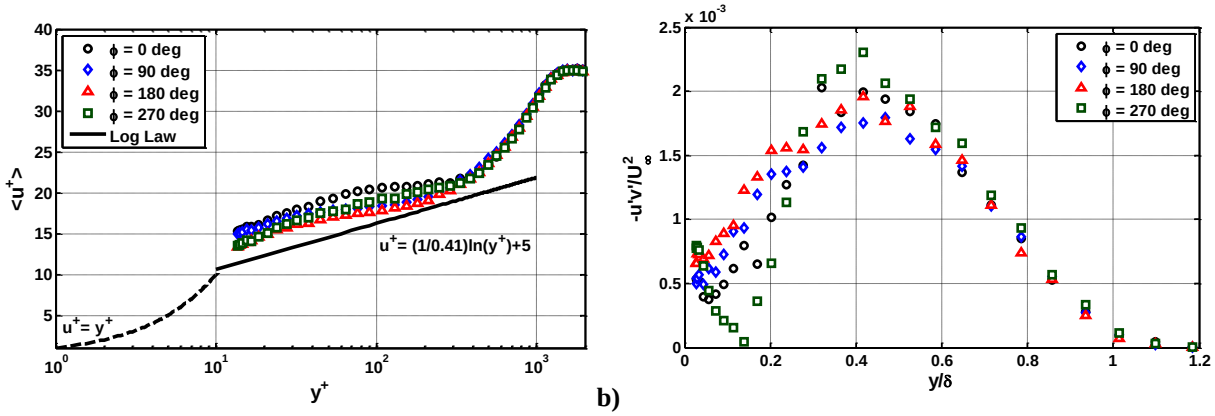

Figure 28. Phase averaged profiles at x/h = 50 for APG with L_o/h = 35.6 and Re_o = 680; a) inner variable scaling velocity and b) Reynolds stress profiles.

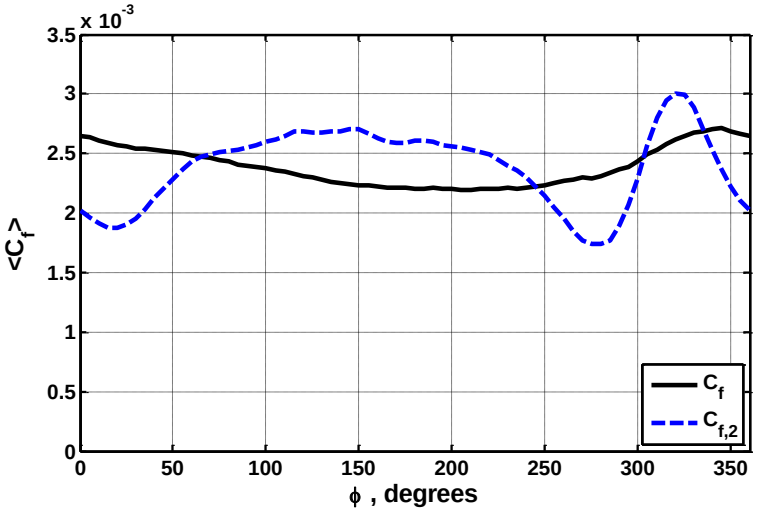

Figure 29. Phase averaged skin friction coefficient at x/h = 50 for APG with L_o/h = 35.6 and Re_o = 680.

One way to analyze the effect of the Reynolds stress on the skin friction of controlled flows is the so called FIK identity presented by Fukagata et al.[19] The FIK identity can be used to decompose the mean skin friction coefficient of wall-bounded turbulent flows into three contributing terms. These sources include the laminar contribution, the turbulent contribution, and the spatial variation of the boundary layer. It provides a direct relation between the skin friction coefficient and the Reynolds stress distribution. For a flat plate boundary layer case, the turbulent contribution to the skin friction coefficient is defined as:[20]

$$C_{f,2} = -4\int_0^1 \frac{u'v'}{U_\infty^2}\left(1-\frac{y}{\delta}\right)d\left(\frac{y}{\delta}\right) \tag{5}$$

This weighted integral approach of the Reynolds stress was applied for the unsteady SJA control case with L_o/h = 35.6 and Re_o = 680. The phase averaged turbulent contribution to the skin friction coefficient is also presented in Figure 29. It is clear that the variation of the turbulent contribution is out of phase with the total skin friction coefficient. In order to investigate this issue further, the streamwise development of the phase average $C_{f,2}$ was calculated for the same actuator and APG boundary layer conditions. These results are presented in a contour plot in Figure 30. The peak blowing originating at x/h = 0 and ϕ = 40°, results in a reduction in the turbulent contribution to the skin friction downstream of slot. The peak suction located at x/h = 0 and ϕ = 220° results in a reduction upstream of the slot. The phase and space contour clearly shows the convection of the effect originating from the blowing portion of the cycle.

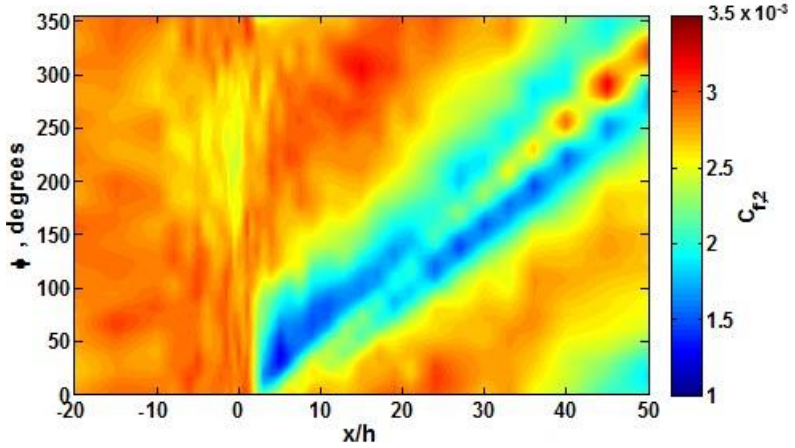

Figure 30. Streamwise contours of the phase averaged turbulent contribution to skin for APG with actuator setting of L_o/h = 35.6 and Re_o = 680.

The streamwise development of the time average turbulent contribution to the skin friction for increasing jet Reynolds number is presented in Figure 31. The velocity profiles for this case clearly showed an increase in the mean skin friction coefficient with jet Reynolds number, but the results here show a reduction in the turbulent contribution as the jet Reynolds number increase. Both the time average and phase average results shows that the mechanism for increased skin friction, which is beneficial for boundary layer separation control, is not due to turbulent coherent structures resulting from the SJA excitation. Rather, it can be concluded that the spatial variation of the boundary layer due to reduction in shape factor and the unsteady forcing of the wall jet are the primary contribution to the increase in skin friction coefficient.

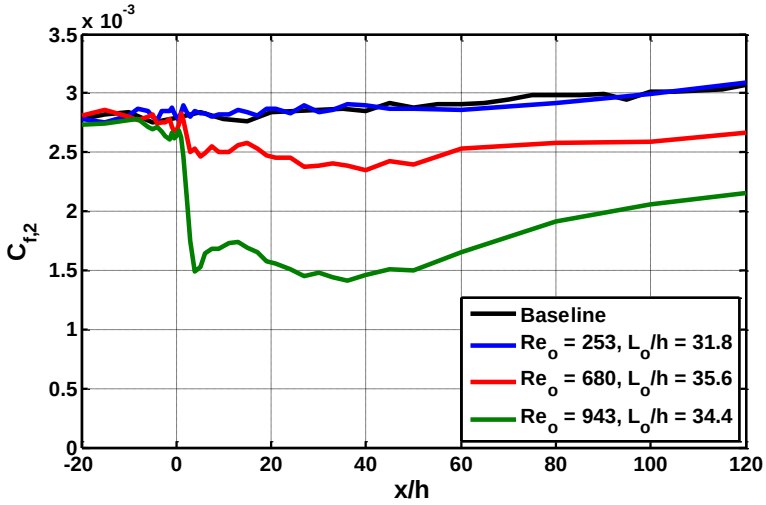

Figure 31. Time averaged turbulent contribution to the skin friction for APG and various Re_o.

V. Summary and Conclusions

This experimental effort generated a comprehensive database of the interaction of two-dimensional ZPG and APG turbulent boundary layers with a synthetic jet actuator. The test matrix considered the SJA parameters of the non-dimensional stroke length, jet Reynolds number, and the angle of the spanwise slot. The selected settings, bounded by the operating limits of the chosen actuator, were used for each slot angle to compare the effect of L_o/h and Re_o independently for quiescent air and the boundary layer flows. Measurements in quiescent air show that each actuator parameter and each spanwise slot angle resulted in distinctly different time averaged and phase averaged flowfields. When cross flow was introduced, the boundary layer control effect was shown to be highly sensitive to slot angle between 90 and 60 degrees. From 60 to 30 degrees there is much less variation as the jet turns and follows the surface just downstream of the slot. Actuation with the 90 degree slot produces a blockage effect on the boundary layer flow, while the angled slots resulted in an attached wall jet.

Further studies of the 45 degree slot were conducted to quantify structural changes to ZPG and APG boundary layer flows. The boundary layer control authority, in terms of momentum addition and shape factor reduction, for a fixed jet Reynolds number and stroke length, decreased with increasing freestream velocity. For a fixed freestream Reynolds number, the results from the ZPG and APG cases both show that, for the range of parameters tested, the boundary layer control is more sensitive to the jet Reynolds number parameter than the non-dimensional stroke length. The resulting profiles of the Reynolds stress distribution and the anisotropy coefficient showed that the turbulent boundary layer flow undergoes structural changes in the time averaged sense due to the SJA excitation. Phase averaged measurements of the boundary layer and SJA interaction captured not only the sequence of the pulsed blowing jet, but also the upstream thinning of the boundary layer due to the suction portion of the cycle.

Synthetic jet excitation is a reliable method for momentum addition and control of near wall turbulent flow. Implementation of SJA or any AFC technology in a real world application will require the extensive use of large scale simulations and a net benefit for the aircraft/rotorcraft from a power perspective. This experimental dataset in a canonical ZPG turbulent boundary layer flow and a mild APG flow provides a validation case for future active flow control simulations. Future studies should consider the interaction of a SJA with a strong adverse pressure gradient

near separation, which is more representative of the operational environment. Additional studies should also consider the internal slot geometry and curvature, input waveform, spanwise segmentation, and multiple streamwise actuator rows. Continuing to explore the link between these parameters and the characteristics of the boundary layer flow, could improve AFC effectiveness and efficiency, which reduces the actuation power required for a certain drag/download reduction specification.

Acknowledgments

The authors would like to thank B. Chan, B. Gesek, S. Nance, W. Peneff, and H. Schwoob of the U.S. Army ADD Wind Tunnel support team. The authors would also like to acknowledge S. Gunatileka for his contributions to the data acquisition program.

References

[1]Martin, P. B., Overmeyer, A. D., Tanner, P. E., Wilson, J. S., and Jenkins, L. N., "Helicopter Fuselage Active Flow Control in the Presence of a Rotor," American Helicopter Society 70th Annual Forum, Montreal, Quebec, Canada, May 20-22, 2014.

[2]Wilson, J., Schatzman, D., Arad, E., Shtendel, T., and Seifert, A., "Active Separation Control Applied to an Axis-symmetric Body," *AIAA Journal*, Vol. 51, No. 10, 2013, pp. 2432-2446. doi: 10.2514/6.2012-72

[3]Glezer, A., and Amitay, M., "Synthetic Jets", *Annu. Rev. Fluid Mech*. Vol. 34, 2002, pp. 503–529.

[4]Smith, B. L., Swift, G. W., "A comparison between synthetic jets and continuous jets." *Experiments in Fluids*, Vol. 34, 2003, pp 467-472. doi: 10.1007/s00348-002-0577-6

[5]Zhang, S., Zhong, S., "Turbulent Flow Separation Control over a Two-Dimensional Ramp Using Synthetic Jets", *AIAA Journal*, Vol. 49, No. 12, 2011, pp. 2637-2649. doi: 10.2514/1.J051046

[6]Wilson, J. S., Martin, P. B., Tung, C., and Tso, J., "Turbulence Measurements of a Two-Dimensional NACA 0036 Airfoil with Synthetic Jet Flow Control," AIAA paper 2006-3157, 24th Applied Aerodynamics Conference, San Francisco, CA, June 5-8, 2006. doi: 10.2514/6.2006-3157

[7]Kim, W., Kim, C., Jung, K. "Separation Control Characteristics of Synthetic Jets Depending on Exit Conditions", *AIAA Journal*, Vol. 50, No. 3, 2012, pp. 559-570. doi: 10.2514/1.J051223 10.2514/1.J051223

[8]Schaeffler, N. W., Allan, B. G., Jenkins, L. N., Yao, C. S., Bartram, S. M., Mace, W. D., Wong, O. D., Tanner, P. E., "Mechanisms of Active Aerodynamic Load Reduction on a Rotorcraft Fuselage with Rotor Effects," AHS Technical Meeting on Aeromechanics Design for Vertical Lift, San Francisco, CA, January 20-22, 2016.

[9]McVeigh, M. A., Nagib, H., Wood, T., Wygnanski, I., "Full-Scale Flight Tests of Active Flow Control to Reduce Tiltrotor Aircraft Download," Journal of Aircraft, Vol. 48, (3), 2011, pp. 786-796. doi:10.2514/1.46956

[10]Schaeffler, N. W., and Jenkins, L. N., "Isolated Synthetic Jet in Crossflow: Experimental Protocols for a Validation Dataset," AIAA Journal, Volt. 44, No. 12, 2006, pp. 2846-2856 doi: 10.2514/1.13743

[11]Jabbal, M., and Zhong, S., "The near wall effect of synthetic jets in a boundary layer", *International Journal of Heat and Fluid Flow*, Vol. 29, 2008, pp 119-130. doi: 10.1016/j.ijheatfluidflow.2007.07.011

[12]Smith, D. R., "Interaction of a Synthetic Jet with a Crossflow Boundary Layer", *AIAA Journal*, Vol. 40, No. 11, 2002, pp. 2277-2288. doi: 10.2514/2.1564

[13]Keirsbulck, L., Labraga, L., and Haddad, M. "Influence of blowing on the anisotropy of the Reynolds stress tensor in a turbulent channel flow", *Experiments in Fluid*, Vol. 40, 2006, pp. 654-662. doi: 10.1007/s00348-005-0105-6

[14]Skare, P. E., and Krogstad, P.A., "A turbulent equilibrium boundary layer near separation," *J. Fluid Mechanics*, Vol. 272, 1994, pp. 319-348. doi: 10.1017/S0022112094004489

[15]Spalart P. R. and Watmuff, J. H., "Experimental and numerical study of a turbulent boundary layer with pressure gradients," *J. Fluid Mechanics*, Vol. 249, 1993, pp. 337-371. doi: 10.1017/S002211209300120X

[16]Bruun, H. H., *Hot-Wire Anemometry: Principles and Signal Analysis*, Oxford University Press, New York, 1995.

[17]Monty, J. P., Harun, Z., and Marusic, I., "A parametric study of adverse pressure gradient turbulent boundary layers," *International Journal of Heat and Fluid Flow*, Vol. 32, 2011, pp. 575-585. doi: 10.1016/j.ijheatfluidflow.2011.03.004

[18]Hussain, A. K. M. F., and Reynolds, W. C., "The mechanics of an organized wave in turbulent shear flow," *J. Fluid Mechanics*, Vol. 41, part 2, 1970, pp. 241-258.doi: 10.1017/S0022112070000605

[19]Fukagata, K., Iwamoto, K., and Kasagi, N., "Contribution of Reynolds stress distribution to the skin friction in wall-bounded flows," *Physics of Fluids*, Vol. 14, No. 11, 2002, pp. 73-76. doi: 10.1063/1.1516779

[20]Deck, S., Renard, N., Laraufie, R., and Weiss, P. E., "Large-scale contribution to mean wall shear stress in high-Reynolds number flat-plate boundary layers up to $Re_\theta = 13650$," *J. Fluid Mechanics*, Vol. 743, 2014, pp. 202-248. doi: 10.1017/jfm.2013.629